Aerospace Science and Technology 136 (2023) 108244

Contents lists available at ScienceDirect

Aerospace Science and Technology

journal homepage: www.elsevier.com/locate/aescte

Initial exploration of a compliance-based morphing fairing concept for hinged aerodynamic surfaces

Nuhaadh Mohamed Mahid *,[1], Benjamin King Sutton Woods [2]

University of Bristol, Queen's Building, University Walk, BS8 1TR, Bristol, UK

ARTICLE INFO

Article history:
Received 4 August 2022
Received in revised form 15 November 2022
Accepted 6 March 2023
Available online 10 March 2023
Communicated by Saravanos Dimitris

Keywords:
Adaptive structures
Morphing skins
Folding wingtips

ABSTRACT

Discontinuity on aerodynamic surfaces leads to notable aerodynamic penalties which could be avoided with compliant fairings. This paper introduces a novel design for a compliant fairing to eliminate the gaps present on hinged aerodynamic surfaces such as hinged wingtips. The fairing is designed to provide a smooth, continuous change in shape between the surfaces on either side of the hinge as they rotate relative to each other. While the concept is generally applicable to any folding surface, including trailing edge flaps, this work focuses on applying it to the Semi-Aeroelastic Hinge (SAH) wingtip concept, which consists of a hinged outer wing panel mounted at a flare angle to the incoming flow. The design aims to minimise the strain on the skin and the rotational stiffness of the fairing while maintaining a smooth and robust outer aerodynamic surface. The skin is attached to the underlying joint structure via a novel pivoting-rib solution which alleviates skin strains over the $+90/-20°$ operating rotation range of the joint. This paper introduces the concept and motivates the design constraints underlying it. A simplified analytical model of the fairing mechanism is presented and the effects of changing the design variables are explored. The results show the benefit of the pivoting ribs over fixed ribs in minimising the strain on the skin and the folding stiffness of the joint. Further arguments are drawn to emphasise the need for a higher fidelity model to account for the geometric and out-of-plane deformation effects of the fairing.

1. Introduction

There has been an increasing emphasis on reducing the fuel consumption of aircraft in general, and in particular commercial airliners, not only to minimize running costs but also to reduce the impact of aviation on climate change. Hence, ways of reducing the induced drag of the wing, including through the pursuit of higher aspect ratios, have increasingly been explored in literature. However, two main unaddressed challenges have long existed in pursuing longer wings; namely,

(1) the limitation on span from the airport gate sizes
(2) and the additional structural requirements from the increased wingspan.

Generally speaking, longer wingspans provide greater range and fuel efficiency whereas shorter wingspans are better for manoeuvrability. Hence, the concepts with the ability to change the wingspan based on the flight phase have been explored in literature. These include span morphing concepts realised through various mechanisms including telescopic spar/panels, scissor extenders and foldable wings. For example, a prototype of the telescopic wing concept has been flown as early as 1931 on MAK-10 aircraft [1]. Scissor extenders are used on the wing box spar along with either sliding or stretchable skin [2]. A span-reducing folding mechanism has been studied in the Agile Hunter concept by Lockheed Martin which folds the inner section of the wing against the fuselage [3]. A comprehensive review of various span morphing concepts can be found in Barbarino et al. [1] and Ajaj et al. [4].

It is noted that the key driver for morphing in military aircraft is to adapt the aircraft for different flight phases to improve its performance. However, the main driver for commercial aircraft is to improve fuel efficiency. This is achieved via a trade-off in favour of reduced induced drag over a slightly higher skin friction drag. The coefficient of induced drag is proportional to the square of the lift coefficient and inversely proportional to the aspect ratio. Hence, the induced drag could be minimised by:

(1) reduced weight via improved structural efficiency which reduces the required lift coefficient,

* Corresponding author.
E-mail addresses: nuhaadh.mahid@bristol.ac.uk (N.M. Mahid), ben.k.s.woods@bristol.ac.uk (B.K.S. Woods).
[1] PhD student, Bristol Composites Institute.
[2] Associate Professor of Aerospace Structures, Dept. of Aerospace Engineering.

https://doi.org/10.1016/j.ast.2023.108244

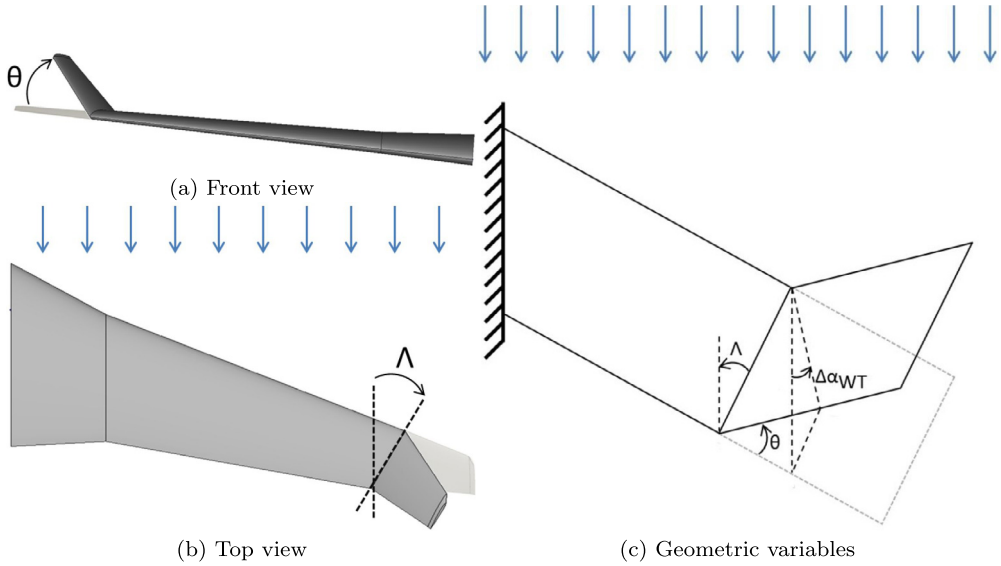

Fig. 1. Semi-Aeroelastic Hinge (SAH) Concept (figures reproduced from Ref. [6]). (a) shows the front view with the folding angle θ, (b) shows the top view with flare angle λ and (c) shows the change in incident angle $\Delta\alpha_{WT}$ of the wingtip as the hinge rotates.

(2) and longer wingspan which increases the aspect ratio, thereby, improving the lift distribution along the span.

The following concept discussed aims to make use of these two features to reduce the induced drag of the aircraft and consequently improve fuel efficiency.

1.1. Semi-aeroelastic hinge concept

Span extension concepts address the challenge of airport gate size; however, they do not provide a mechanism to circumvent the additional structural requirement of the increased bending moment from a longer wing. One of the approaches which address both the challenges is the Semi-Aeroelastic Hinge (SAH) concept introduced by Siddaramaiah et al. [5], which is shown in Fig. 1. It shows a wingtip that is pivoted to the inboard wing via a free/flexible hinge. The hinge is oriented at a flare angle λ from the freestream. For a positive flare angle, upward folding of the wingtip by a positive folding angle θ geometrically reduces the incident angle of the wingtip α_{WT}. This change in the incident angle of the wingtip is expressed by

$$\Delta\alpha_{WT} = -\tan^{-1}(\tan\theta \sin\lambda) \tag{1}$$

A reduced angle of incidence on the wingtip reduces the lift generated at the outboard sections of the wing. This reduces the bending moment transferred to the inboard sections of the wing. In steady flight, the balance of aerodynamic and gravitational moments on the hinge, from the wingtip, leads to an equilibrium folding angle, also referred to as the coasting angle. However, when exposed to gust loading, the wingtip is able to flap up and down – providing load alleviation characteristics leading to reduced peak loads on the inboard wing. Consequently, the concept provides a mechanism to achieve an extension of the wingspan with minimal additional reinforcement required on the primary load-carrying structure of the wing.

The gust load alleviation behaviour of the SAH concept along with the parameters which optimise that aspect of the wingtip have been studied in previous literature. Siddaramaiah et al. [5] showed that for a wingtip hinged at 80% of the span on a typical jet airliner size aircraft (with 57.82 m wingspan and weighing 190 tonnes), low torsional stiffness and high flare angle of the hinge increase the achieved gust load alleviation compared to the hinge-less baseline wing. For example, a hinge flared at a 25-degree angle was shown to reduce the root bending moment by 15% under static loading and by 19% under gust loading compared to the hinge-less wing. The benefit of extending the wingspan by 25%, using the SAH concept has further been demonstrated by Castrichini et al. [7]. It was shown that a hinge with low torsional stiffness and flare angle of 25 degrees reduced the wing root bending moment by 30% compared to a fixed hinge; and increased the wing root bending moment by only 4.4% compared to the baseline wing without the wingtip, despite the increased span of 25%. It was also shown that the gust load alleviation is improved by high flare angle, low torsional stiffness, low wingtip mass and low damping.

In short, the SAH concept enables span extension while maintaining a light design for the wing structure. To achieve both the benefits of the SAH concept, the wingtip would need to be fixed in steady flight at zero folding angle for the greatest effective wingspan, and deployed in response to gusts for load alleviation. This would require a clutch mechanism to release the wingtip and an actuator to return the wingtip to zero folding angle.

1.2. Fairing

Despite the benefits of the SAH concept, it also poses challenges due to the inherent discontinuity of the aerodynamic surface across the hinged joint as seen in the wind tunnel model in Fig. 2. The gap distorts the airflow across the wing – leading to aerodynamic penalties. In a configuration with zero flare angle, which has the discontinuity of the aerodynamic surface aligned with the airflow, the presence of an exposed hinge within the gap will create vortices leading to reduced lift and increased drag. Alternatively, in a configuration with a non-zero flare angle, the gap will be misaligned to the airflow leading to even more convoluted three-dimensional flows with increased pressure drag. Hence, without a cover around the hinge vortices and the subsequent flow separation on the wing will partially erode the aerodynamic benefit of the extended wingspan. Furthermore, the presence of a gap in the wing surface would likely increase the likelihood of ingestion of debris and subsequent damage to the hinge components, particularly during take-off and landing.

Mechanical solutions to covering this gap could include overlapping/sliding skin panels or a cylindrical cover on the hinge with

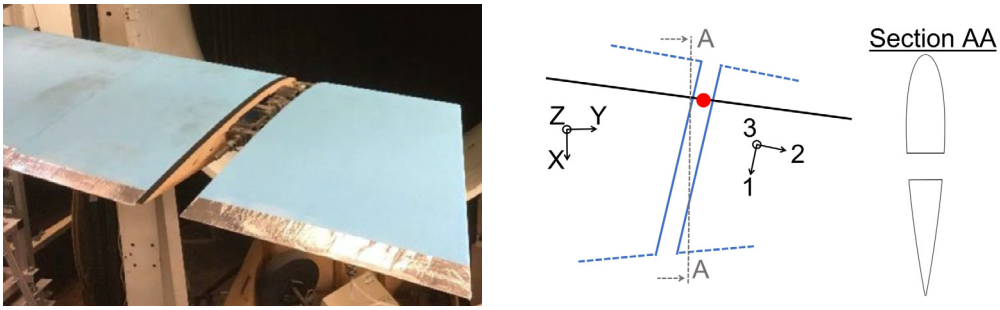

(a) Wind-tunnel model (b) Schematic of the joint

Fig. 2. SAH joint between the inboard wing and the wingtip. (a) shows the gap at the joint in a wind tunnel model (figure reproduced from Ref. [8]) and (b) shows the schematic of the joint region. Axes XYZ is the global coordinate system where X is aligned with freestream. Axes 123 is the local coordinate system where 1-axis is in the direction along the hinge and 2-axis is the direction across the hinge. Section AA shows the surface discontinuity in the aerofoil section created by the hinge gap.

a socket-shaped joint interface on the wingtip. However, such solutions will not provide a smooth continuous surface due to overlaps and protuberances of the surface components, and would be mechanically complex with multiple sliding interfaces requiring sealing. The general benefits of replacing rigid mechanisms with morphing concepts capable of continuous and smooth changes in surface curvature have been demonstrated by various morphing concepts explored in literature. For example, Woods et al. [9] showed a 3% reduction in wing drag and a 7% increase in the lift to drag ratio through the closure of the spanwise gap between the aileron and the wing. The aerodynamic gain of a continuous skin with a smooth curvature is presumed to be even greater for the SAH concept which has a gap across the wing from the leading edge to the trailing edge, which is likely to be skewed relative to the flow.

A compliant fairing around the joint would close the gap and create a continuous smooth outer surface for the airflow. The mechanical properties of such a fairing are constrained by the need to maintain the aerodynamic shape, undergo the required range of deformation and optimise the load alleviation characteristics of the wingtip. The subsequent sections of this paper initially introduce the requirements of the fairing, followed by a categorical description of two different concepts for skin integration. The more promising of the two concepts is pursued further with a simplified analytical study to identify the key design drivers and constraints. Further changes to the design are proposed to address the constraints identified and arguments are drawn to emphasise the need for higher fidelity analysis to capture the effects of the complex three-dimensional geometry.

2. Requirements of the fairing

The requirements of the fairing are based on various characteristics including the operational range, aerodynamic shape of the wing, gust load alleviation and structural longevity. They are broken down into three categories: structural, aeroelastic and operational requirements.

2.1. Structural

In the SAH concept, the wingtip is envisioned to rotate in the range of $-20°$ to $90°$ of folding angle. While the lower limit is set by the ground clearance required for the wingtip, the upper limit is based on achieving the maximum shortening of the wingspan. The large range of folding angle implies that the fairing around the hinge would strain extensively in the direction across the hinge (i.e. 2-axis direction in Fig. 2b). Generally speaking, isotropic materials that have high strain before failure, such as elastomers, typically have a high Poisson's ratio. With such materials as a fairing, an in-plane deformation in the direction across the hinge would also result in deformation in the direction along the hinge. This would distort the cross-section (aerofoil) shape of the wing leading to drag penalties and loss of lift due to unfavourable aerodynamics on the surface. Hence, it is required that the fairing has a near-zero Poisson's ratio in the direction along the hinge to minimise the distortion of the cross-section shape. Additionally, the fairing would have to carry out-of-plane loading from the aerodynamic pressure at transonic cruise conditions. Hence, a high out-of-plane stiffness is required on the fairing to reduce the aerodynamic penalty due to the distortion of the cross-section shape. A maximum limit on the out-of-plane deformation of the skin could be used to determine the required out-of-plane stiffness. Such deformation limits should consider the drag increase due to distortion of the cross-section shape.

2.2. Aeroelastic

As load alleviation is one of the key features of the SAH concept, the properties of the fairing should either favour or at least not hinder the gust load alleviation behaviour of the wingtip. The properties which optimise the gust load alleviation characteristics are summarised as high flare angle, low torsional stiffness, low damping and minimal mass [5,7]. For the fairing, the low torsional stiffness of the joint translates to a low in-plane stiffness in the direction across the hinge. Other variables which affect the torsional stiffness through the effective moment arm around the hinge, include the distance of the fairing from the hinge and the thickness of the fairing. These variables are constrained by the cross-section shape of the wing and the out-of-plane stiffness requirement of the fairing respectively. Hence, a trade-off would need to be made between these competing requirements to obtain an optimised solution. Moreover, a minimum constraint is also required on the torsional stiffness of the joint to avoid flutter of the wingtip within the operating speeds of the aircraft [7]. This would mean that the fairing designer would need to consider not only the elastic and aerodynamic aspects of the wingtip but also the aeroelastic behaviour as well. Noting that the total torsional stiffness of the joint is the combined contribution from both the hinge and the fairing, hereafter, the total torsional stiffness of the joint is referred to as the folding stiffness.

2.3. Operational

The gust load alleviation behaviour of the wingtip entails repetitive flapping motion of the wingtip. This results in cyclic loading on the components of the hinge in addition to the fairing itself. Hence, it is required that the materials selected for these components have high fatigue life and/or the components themselves are

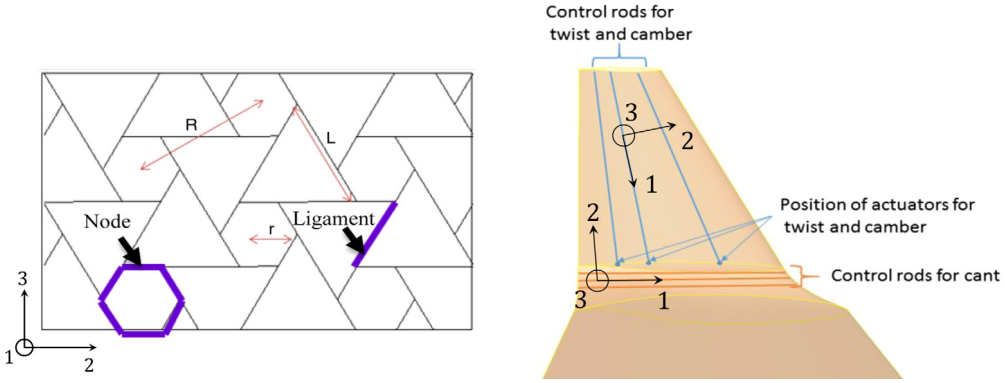

(a) Face view of the cellular core (b) Orientation of the core

Fig. 3. An example of a primary morphing structure based on a chiral cellular core with a facesheet (figures reproduced from Ref. [10]). (a) shows the face view of the cellular core and (b) shows the orientation of the core (using the 123 axes) in the folding region and the wingtip, along with their control rods.

easily accessible for replacement if required to be changed within the lifespan of the aircraft. Moreover, the materials of the fairing are required to be durable with minimal corrosion and degradation due to the operating conditions. Durability includes thermal and chemical stability along with resistance to impact damage from debris – particularly during take-off and landing. Additionally, the fairing design is required to be cost-effective both in its manufacture and maintenance. This is to increase the attractiveness of the morphing solution over a conventional mechanical solution, to address the surface discontinuity of the SAH concept.

3. Design approaches

Taking a step back from the SAH concept, there are various ways of realising a compliant folding wingtip. Categorically, designs of such a device can be broken down into two: (1) primary morphing devices and (2) secondary morphing devices. These two categories differ in the way they carry the internal loads and consequently in the way the structure of the joint interact with the other functional components of the joint.

3.1. Primary morphing structures

In primary morphing devices, the entire structure undergoes a change in shape upon loading. The morphing joint not only carries the pressure load on its surface but also transfers the load from the wingtip to the inboard wing. In this case, the morphing joint structure is the only load path between the wingtip and the inboard wing. A realisation of a primary morphing device could simply be a block of flexible material between the wingtip and the inboard wing. These materials could include elastomers, cellular structures with smooth facesheets and smart materials such as shape memory polymers.

An example of a primary morphing device concept introduced by Cooper et al. [10], is shown in Fig. 3. It shows a morphing wingtip that is connected to the inboard wing via a morphing joint. Both the wingtip and the joint are comprised of a chiral cellular core with a bonded surface layer. The chiral core can be deformed either by rotating a node or shortening a ligament (see Fig. 3a). In this application, the core is deformed by rotating a combination of nodes. Hence, for the joint, the core is oriented with the axis of rotation of nodes aligned parallel to the folding axis of the wingtip. The control rods for cant, shown in Fig. 3b, are then used to actuate the folding of the wingtip. Additionally, rods are also placed along the wingtip which are used to change the camber and the twist of the wingtip panel.

In primary morphing structures, the functions of aerodynamic surface and spanwise load path are performed by a single integrated structure. This reduces part count with a potential reduction in production and maintenance costs. However, a single integrated structure is unlikely to have adequate de-coupling between the folding stiffness of the joint and the out-of-plane stiffness of the surface. Hence, a typical primary morphing structure that is adequately resistant against deformation of the wing surface under pressure loading, is likely to also have high bending (folding) stiffness. This is equivalent to high torsional stiffness in the joint which, as discussed in the introduction, results in reduced ability of the wingtip to alleviate gust load.

Primary morphing structures using smart materials such as shape-memory polymers have the benefit of being able to perform the function of deployment and retraction of the wingtip without the need for additional actuators. The limitation, however, is that the response of shape-memory materials is often too slow – making it unsuitable for gust response which requires the instant deployment of the wingtip. Moreover, most of the shape memory materials are stimulated via temperature change either using thermal or electrical energy. Such elements would require insulation due to the storage of fuel in the wing and the high rate of convective cooling at the wing surface. This would increase the complexity of the design making it less attractive than a more conventional mechanical solution.

3.2. Secondary morphing structures

Secondary morphing devices have separate structural components to carry the loads from the wingtip to the inboard wing and the aerodynamic loads on the surface of the fairing around the joint. In the simplest case, a secondary morphing device could be realised as a hinged joint, similar to the one shown in Fig. 2a, with an elastomeric fairing joining the skin of the inboard wing and the wingtip. In this case, the joint will carry the shear loads from the wingtip to the inboard wing while the fairing will carry the pressure loads on the surface of the joint section.

The joint is comprised of relatively stiff materials whereas the fairing would require its stiffness properties to be directionally tailored to meet the functional needs. These include low in-plane stiffness across the hinge for better load alleviation – and high in-plane stiffness along the hinge and high out-out-plane stiffness throughout for better aerodynamics. Additionally, the fairing material is also required to endure high levels of recoverable strain to achieve a 90-degree folding angle. These requirements are unlikely to be met with monolithic structures, thereby motivating the need for more tailored solutions.

The secondary morphing structural concept proposed in this work is shown in Fig. 4. It shows a spanwise beam connecting the inboard wing and the wingtip via a hinged joint. Note that

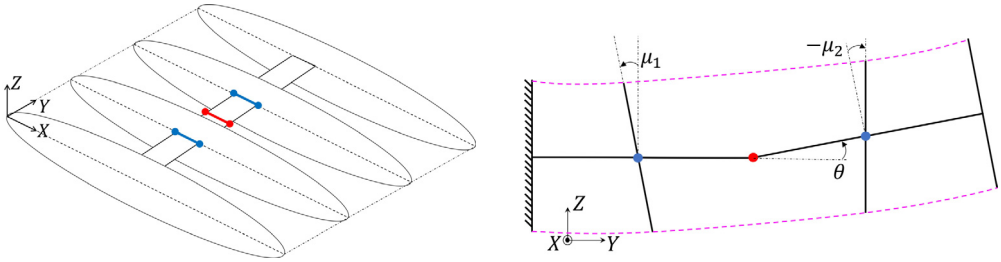

(a) Isometric view of the joint (b) Rear view (YZ-plane) of the joint

Fig. 4. An example of a secondary morphing structure for a hinged wingtip. (a) shows the joint connecting the inboard wing and the wingtip. (b) shows the rear view (YZ-plane) of the joint at a folding angle of θ and rib rotation angles of μ_1 and μ_2. In both the subfigures, the hinge which rotates the wingtip is shown in red and the hinges pivoting the ribs are shown in blue. (For interpretation of the colours in the figure(s), the reader is referred to the web version of this article.)

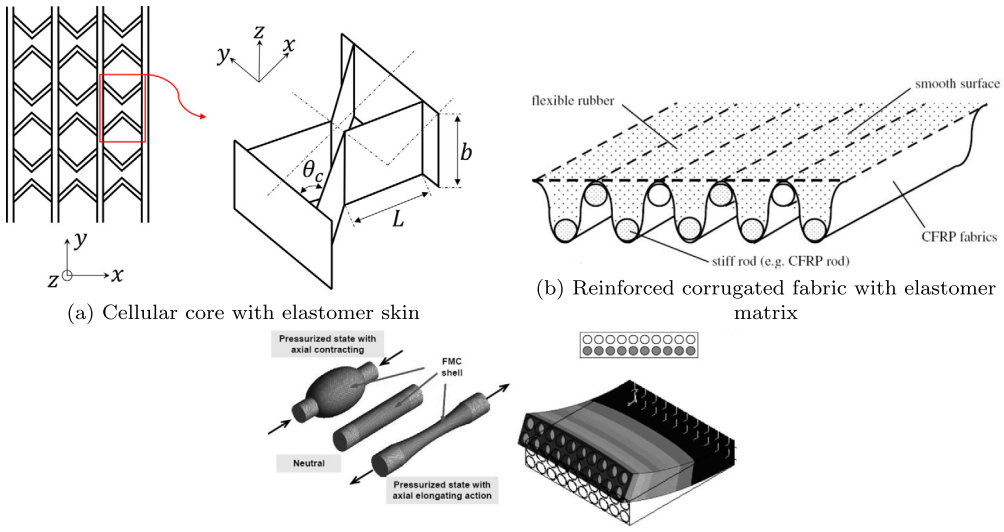

(a) Cellular core with elastomer skin (b) Reinforced corrugated fabric with elastomer matrix

(c) Fluidic, flexible matrix composite

Fig. 5. Examples of potential skin architectures for morphing fairings extracted from literature. (a) shows a chevron based cellular structure sandwiched between elastomer layers [13]. (b) shows an elastomer-filled panel with a corrugated carbon-fibre sheet and carbon-fibre rods along the corrugation channels (figure reproduced from Ref. [14]). (c) shows an elastomeric matrix with an embedded network of fluidic pneumatic actuators (figure reproduced from Ref. [15]).

this beam is of notional thickness in the schematic – but would of course be designed and sized accordingly in a real implementation. Due to the presence of a hinge, this configuration minimises the transfer of bending moment from the wingtip to the inboard wing, assuming that the in-plane stiffness of the skin in the direction across the hinge is low. The ribs in the joint are hinged to the spanwise beam allowing them to rotate. The axes of rotation of the ribs are parallel to the axis of rotation of the folding hinge. The rotation of the ribs allows the deformation of the skin due to the folding of the wingtip, to be distributed over a greater length of skin. For instance, consider the compressive deformation on the top skin in the central rib-bay, shown in Fig. 4b. The rotation of the ribs by the angles μ_1 and μ_2 results in compressive deformation of the top skin of the central rib-bay being partially re-distributed to the top skin of the adjacent rib-bays. This re-distribution of deformation over a longer length of the skin is a key aspect of this concept as it results in a lower maximum strain on the skin.

A few examples of potential skin architectures extracted from literature are shown in Fig. 5. A more expansive review of morphing skin designs along with the skin architectures discussed here can be found in Thill et al. [11].

A sandwich panel comprised of a patented chevron-based cellular core [12] known as MorphCore and elastomer facesheets [13], used in span extension devices is shown in Fig. 5a. It shows the ribs along the y-axis which provide the near-zero Poisson's ratio and the chevron walls which bend to provide high flexibility along the x-axis. Similarly, Fig. 5b shows an elastomer-filled corrugated sheet that is flexible across the corrugation – and rods along the corrugation channel which provides near-zero Poisson's ratio [14]. In this configuration, the skin would become significantly stiffer when the corrugation is fully extended. In a fairing with this skin, the corrugation channels would be aligned parallel to the hinge axis. Hence, the stiffening of the skin due to full extension of the corrugation could be used to stop the wingtip folding beyond the pre-defined maximum folding angle.

An alternative configuration, in Fig. 5c, shows an elastomer-based matrix with an embedded fluid-filled network of pneumatic actuators [15]. In a fairing with this skin, the pressure in the tube could be varied to change the folding stiffness to deploy the wingtip. Differential pressure can also be applied within the network of pneumatic actuators to return the wingtip to the planform position. This will allow the skin to be used as an actuator.

The benefit of a secondary morphing concept is in its ability to minimise the coupling between the folding stiffness of fairing and the out-of-plane stiffness of the skin. This decoupling is essential due to the competing requirements of the two parameters to optimise load alleviation while maintaining a robust cross-section shape of the wing. Additionally, the secondary morphing concept is more space-efficient and provides more room within the joint for other components that may be required for the operation of the SAH concept, such as clutches and actuators. This would minimise, if not completely avoid, the need for increasing the thickness of the wing profile around the joint to add internal space – thereby, avoiding the drag penalty this would incur.

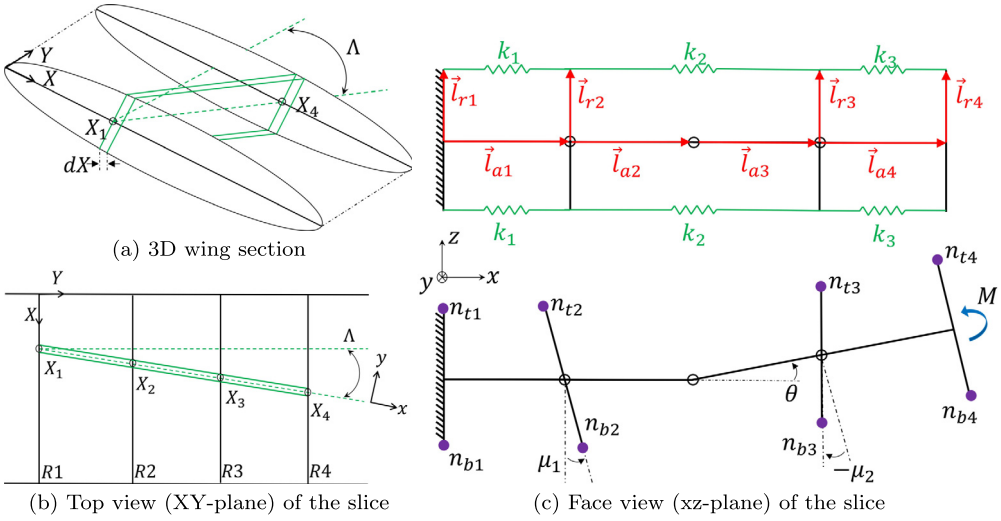

Fig. 6. Simplification of the fairing geometry. (a) shows the 3D joint along with the 2D slice shown in green. (b) shows the top view for the joint with the rib locations of the slice annotated as X_i for $i \in [1, 4]$. Note that the global coordinate system is annotated as axes XYZ and the local coordinate system on the slice is annotated as axes xyz. (c) shows the face view of the slice along with the annotations for the variables. n_{ti} and n_{bi} are node locations on the top and bottom surface respectively, and l_{ri} and l_{ai} are the rib heights and beam lengths respectively. k_i for $i \in [1, 3]$ are the linear springs modelling the skin stiffness.

The drawback of the secondary morphing structure is the increased part count and the complexity of the design. However, a modular approach to design would allow for the replacement of parts when needed instead of the whole joint. Moreover, reduced weight and wetted area of the joint with its performance benefits could be a trade-off against the increased complexity of the design.

4. Analytical model of morphing fairing structure

The secondary morphing concept based on a hinged joint and pivoting ribs, was selected as the most promising and is, therefore, the focus of the rest of this paper. The choice of this concept is based on its ability to minimise coupling between the folding stiffness of the fairing and the out-of-plane stiffness of the skin, in addition to its space efficiency which minimises the need for a local increase in the wing thickness around the joint.

4.1. Objectives

The objective of the analytical model developed here is to capture the basic mechanics of the fairing, using various simplifying assumptions, in order to allow for initial exploration of the design space and to determine the basic viability of the concept. Specifically, it should demonstrate the deformation mechanics and the ability of the pivoting-rib configuration to re-distribute the skin deformation to adjacent rib bays to minimise the localised strain on the skin. The model is also used to demonstrate the effects of various geometric parameters on the folding stiffness and the deformed shape of the joint.

4.2. Geometry simplification

The complex 3-dimensional geometry of the fairing with non-planar skin curved around the ribs makes an analytical solution impractical for the full model. Hence, as a preliminary approach, the model is simplified to a 2-dimensional problem by taking a slice of the fairing across the hinge as illustrated in Fig. 6. It shows the slice of infinitesimal thickness dX taken at an angle λ from the spanwise direction which ensures that the face of the slice is perpendicular to the hinge axis. Note that the flare angle λ is measured from the freestream (see Fig. 1), hence, in this case, it is assumed that the wing has no sweep. Fig. 6b shows the top view of the wing section along with the global coordinate system and the local coordinate system of the slice. Note that from hereon, for clarity, the local x-direction (lower case implies local coordinates, upper case is global) is referred to as the axial direction and the local y-direction is referred to as the transverse direction. The transverse direction is parallel to the hinge axis while the axial direction is perpendicular to it. Fig. 6c shows the face view of the slice along with the annotation of the variables. The skin panels are modelled as linear springs to capture their in-plane stiffness. This approach does not account for the bending deformation or through-thickness shear effects of the fairing. However, this approach is deemed adequate for this initial study which is not intended to capture out-of-plane behaviour or the interaction of aerodynamic loads with the skin. This simplified approach allows the objectives of this study to be achieved via a numerically solvable set of equations that does not require a finite element based approach.

4.3. Model derivations

The stiffness of the skin of the fairing is modelled as linear springs and is expressed by

$$k_i = \frac{E_x(t\,dx)}{L_i} = \frac{Q}{L_i} \tag{2}$$

where E_x is the Young's modulus in the axial direction, t is the thickness of the skin and L_i is the undeformed length of the skin. The slice is normalised by its thickness, hence, dX is simply assumed to be 1. Q is the product of Young's modulus and the cross-section area, which in this analysis are the same for all skin sections. Hence, the difference between the stiffness of the skin sections is only due to their length.

The location of each rib that intersects with the slice is annotated in Fig. 6b as X_i where $i \in [1, 4]$. X_i gives the chordwise location of the rib at the intersection with the slice and is evaluated by

$$X_2 = X_1 + l_{a1}\sin\lambda, \quad X_3 = X_1 + \sum_{i=1}^{3} l_{ai}\sin\lambda,$$
$$X_4 = X_1 + \sum_{i=1}^{4} l_{ai}\sin\lambda \tag{3}$$

Once the chordwise location of the intersection is known, the rib height l_{ri} for $i \in [1, 4]$ is evaluated for the aerofoil used.

The deformation of each skin section is given by the change in the distance between the adjacent nodes n_{ti} and n_{bi} for $i \in [1, 4]$. A vector-based approach is used to evaluate the change in the nodal distances. The vectors used are of the form $\vec{l_{ri}} = [0\, l_{ri}]^T$ and $\vec{l_{ai}} = [l_{ai}\, 0]^T$ where l_{ri} and l_{ai} corresponds to the length of ribs and beams respectively. The position of each node is expressed as a function of the angles θ, μ_1 and μ_2 by the expressions

$$\begin{aligned}
n_{t1} &= \left[\vec{l_{r1}}\right] \\
n_{b1} &= \left[-\vec{l_{r1}}\right] \\
n_{t2} &= \left[\vec{l_{a1}}\right] + \mathbf{R}(\mu_1)\left[\vec{l_{r2}}\right] \\
n_{b2} &= \left[\vec{l_{a1}}\right] + \mathbf{R}(\mu_1)\left[-\vec{l_{r2}}\right] \\
n_{t3} &= \left[\vec{l_{a1}} + \vec{l_{a2}}\right] + \mathbf{R}(\theta)\left[\vec{l_{a3}} + \mathbf{R}(\mu_2)\vec{l_{r3}}\right] \\
n_{b3} &= \left[\vec{l_{a1}} + \vec{l_{a2}}\right] + \mathbf{R}(\theta)\left[\vec{l_{a3}} - \mathbf{R}(\mu_2)\vec{l_{r3}}\right] \\
n_{t4} &= \left[\vec{l_{a1}} + \vec{l_{a2}}\right] + \mathbf{R}(\theta)\left[\vec{l_{a3}} + \vec{l_{a3}} + \vec{l_{r4}}\right] \\
n_{b4} &= \left[\vec{l_{a1}} + \vec{l_{a2}}\right] + \mathbf{R}(\theta)\left[\vec{l_{a3}} + \vec{l_{a3}} - \vec{l_{r4}}\right]
\end{aligned} \tag{4}$$

where $R(\phi)$ is the counter-clockwise rotation matrix for any angle ϕ.

The deformed length of the skin sections L_{ji} is given by the expression

$$L_{ji} = n_{j(i+1)} - n_{ji} \quad \text{where} \quad j \in [t, b] \quad \text{and} \quad i \in [1, 3] \tag{5}$$

where the subscripts t and b correspond to top and bottom respectively (as shown in the node labels in Fig. 6c). Note that the deformed lengths of the skin sections are a function of the angles θ, μ_1 and μ_2. The displacement of the skin sections is evaluated by subtracting the undeformed length of the skin from the deformed length. The displacement of the skin due to any applied pre-strain ϵ_p which may be added to help avoid buckling and to increase the skin's out-of-plane stiffness [16] is also added to the displacement. The expression for the total displacement of the skin section u_{ji} is given by

$$\begin{aligned}
u_{ji} &= \big(L_{ji}(\mu, \theta_1, \theta_2) - L_{ji}(0, 0, 0)\big) + u_{p\,ji} \\
\text{where} \quad u_{p\,ji} &= \frac{\epsilon_p\, L_{ji}(0, 0, 0)}{1 + \epsilon_p}
\end{aligned} \tag{6}$$

Noting that the ribs and beams are assumed in this work to be rigid, the only energy-storing components in the model are the skin sections. Using the stiffness of the individual skin sections and their displacements, the elastic strain energy U of the system is expressed by

$$U = \sum_{i}^{3} \frac{1}{2} k_i \left(u_{ti}^2 + u_{bi}^2\right) \tag{7}$$

The work done W on the fairing by the applied moment M shown in Fig. 6c, is given by

$$W = M\theta \tag{8}$$

The total energy of the system is then expressed by

$$\Pi = U - W \tag{9}$$

Using the principle of minimum energy, the equilibrium solution is given by the Jacobean of the total energy $\nabla\Pi$ with respect to the angles θ, μ_1 and μ_2 where $\nabla\Pi(\theta, \mu_1, \mu_2) = 0$. This equilibrium case is expressed by a set of three nonlinear equations which are solved numerically for the angles θ, μ_1 and μ_2 for any applied moment M. The solution process is executed in MATLAB using the built-in "fsolve" function which by default uses the Trust-Region-Dogleg Algorithm [17]. The stability of the obtained equilibrium solution is given by the eigenvalues of the Hessian matrix of total energy $\nabla^2\Pi$ with respect to the angles θ, μ_1 and μ_2.

Table 1
Default Model Parameters.

Parameters	Details
Wing	NACA 0015 aerofoil with 1.5 m chord and zero flare angle
Slice location	X_i at 40% of the chord
Skin stiffness	$Q = 1000$ N
Beam lengths	250, 100, 100 and 250 mm for l_{ai} were $i \in [1, 4]$ respectively

4.4. Parameters for representative analysis case

An exploration of the fairing design space was carried out using this analysis approach and a nominal aircraft wing with a NACA 0015 aerofoil and a chord of 1.5 m. The choice of a symmetric aerofoil helps to simplify the analysis as it allows pre-strain to be applied on the skin without causing a rotation of the wingtip. The chord length chosen is approximately the typical tip chord of commercial aircraft with just under 36 m wingspan (e.g., A320 and B737-MAX). These aircraft use the airport gates with a wingspan limit of 24 m to 36 m (i.e., Code C in ICAO Annex 14 [18] and Group III in FAA Advisory Circular 150/5300-13B [19]). Hence, any further increase in wingspan without folding wingtips will require them to use a bigger airport gate.

The representative 2D slice was taken starting from the first rib intersection point X_1 at 40% of the chord. Note that the default case was set to have zero flare angle. Any change in flare angle changes the point of intersection of each subsequent rib on the selected slice (i.e. X_i for $i \in [2, 4]$). This results in a change in the chordwise location at which the rib height is evaluated. Hence, the change in flare angle changes the height of the ribs in the slice.

A representative value for the stiffness parameter of $Q = 1000$ N was chosen. This is equivalent to having the skin made of a typical polymer with a Young's modulus of 1000 MPa and a skin thickness of 1 mm. Pre-strain on the skin was set to 15% to avoid negative strain on the compressive side. While the model will be able to consider compressive strain, the predicted results would be inaccurate as there is a likelihood of skin buckling under compressive stress which the model will not be able to account for. Hence, an upper limit on the folding angle was set before the strain on the top skin becomes negative. Consequently, in this study, deformation is shown up to a folding angle θ of 30 degrees for all of the cases considered, except for the study of pre-strain. The model parameters for the analysis are summarised in the Table 1. The choice of slice location, skin stiffness and beam lengths used are arbitrary.

The analysis was run with variations in four primary design parameters of interest: (1) the stiffness of the skin, (2) the flare angle, (3) the applied pre-strain and (4) the length of the spanwise beams. Additionally, an analysis was also run to compare the (5) effects of fixed versus pivoting ribs. The results of these analyses are discussed in the following section of the paper.

5. Results and discussion

The results presented here for the deformation behaviour analysis of the 2-dimensional slice give qualitative insights into the behaviour which would be expected of the 3-dimensional model of the fairing. Particularly, the changes in the deformation response due to changes in different parameters give insights into the rela-

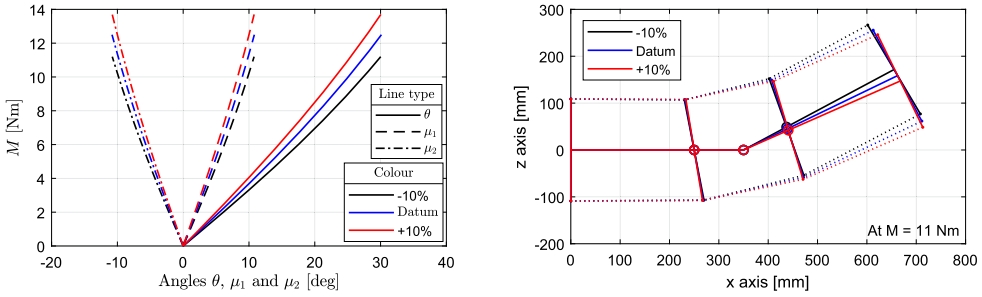

(a) Equilibrium plot (b) Deformed shape

Fig. 7. Variation of the folding stiffness and the deformed shape with the change in skin stiffness. (For interpretation of the colours in the figure(s), the reader is referred to the web version of this article.)

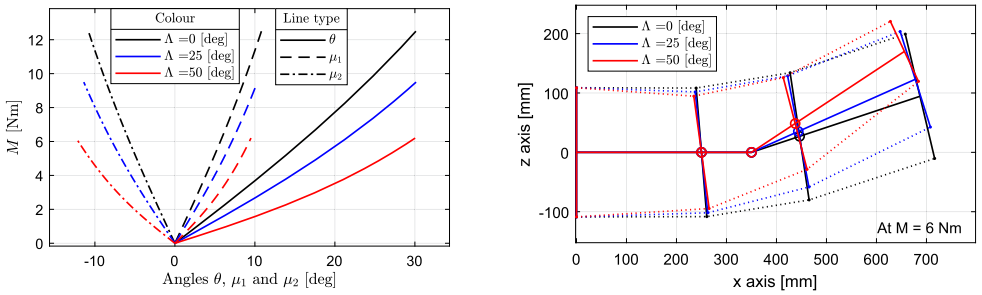

(a) Equilibrium plot (b) Deformed shape

Fig. 8. Variation of the folding stiffness and the deformed shape with the change in flare angle. (For interpretation of the colours in the figure(s), the reader is referred to the web version of this article.)

tionship between the design parameters and the folding stiffness, along with their sensitivities.

5.1. Skin stiffness

Firstly, the effect of varying the stiffness of the skin is shown in Fig. 7. The stiffness was varied by changing the stiffness parameter Q by $\pm 10\%$. Fig. 7a shows the deformation response of each of the cases for varying applied moments. Comparing the cases shows that increasing the stiffness of the skin increases the folding stiffness of the fairing and the rotating stiffness of the ribs. Additionally, for each case, it shows a mild stiffening at higher folding angles. This is indicative of the geometric nonlinearity of the folding stiffness. Moreover, the rotation of the ribs is of equal magnitude but in opposite directions. This is due to the symmetry of the geometry about the folding hinge axis for the cases with zero flare angle.

The shapes of the deformed fairing slice are shown in Fig. 7b. It shows that as the fairing folds up, the distance from the folding hinge to the lower skin decreases while the distance to the upper skin increases. The change in the distance from the folding hinge to the upper and the lower surface is also affected by the rotation of the ribs. The fact that the hinge moves closer to the bottom skin, however, is not intrinsically a problem, as long as the skin is thin enough to not directly come into contact with the hinge. Indeed, this motion indicates that the fairing is working as intended – it is spreading out the single localised point of rotation on the mechanical hinge into a more distributed (albeit still faceted) shape for the skin. This spreading of the deformation is desirable in maintaining a smoother surface to minimise interference drag between the wing and wingtip. Additionally, the folding rotation of the joint also results in a slight decrease in the local thickness of the slice across the hinge. In a 3-dimensional fairing, this is equivalent to decreasing the thickness of the aerofoil section in the folding region. These effects are discussed further later in this paper with the results of the analysis comparing the fixed and pivoted ribs.

5.2. Flare angle

For the second set of studies, the effect of changing the flare angle of the hinge on the deformation response of the fairing slice was analysed in Fig. 8. Fig. 8a shows a significant drop in the folding stiffness of the fairing slice as the flare angle was increased. This is attributed to the taper of the rib height for increasing flare angle, which is shown in Fig. 8b. This is simply an effect of the modelling simplification in which only a thin slice of the wing section is modelled instead of the whole wing section. Hence, for any slice rib position of X_1, each consecutive slice rib position is further aft of the previous rib position (i.e., $X_i > X_{i-1}$ for $i \in [2, 4]$) for any flare angle greater than zero (see Fig. 6b). Noting that the maximum thickness of NACA 0015 is at 30% of the chord and X_1 is set to be at 40% of the chord, each consecutive rib height will be smaller due to the decreasing aerofoil thickness towards the trailing edge.

The decrease in the rib height results in a decrease in the moment arm from the folding hinge to the skin. As the contribution of the moment arm to the folding stiffness is proportional to the square of the moment arm (i.e. $k_{folding} \propto {l_{arm}}^2$), a small decrease in the rib height results in a significant softening of the folding stiffness. Fig. 8a also shows an increase in the difference between the magnitude of the rib folding angles μ_1 and μ_2. This is attributed to the break in the symmetry about the folding hinge axis for non-zero flare angles and the subsequent increase in asymmetry as the flare angle increase. Additionally, the figure shows that the magnitude of μ_2 is greater than that of μ_1 for all values of applied moment. This is a result of rib height taper which gives the outboard rib a lower effective rotational stiffness due to the reduced moment arm from the hinge to the skin.

A noticeable change in the gradient of the folding angle curve is also seen in Fig. 8a, as the applied moment increases, particularly for the case with a 50-degree flare angle. This nonlinear behaviour is seen in the deformation response of all the cases but to a lesser extent. The increase in the gradient of the folding angle curve is indicative of the stiffening of the fairing at higher folding angles.

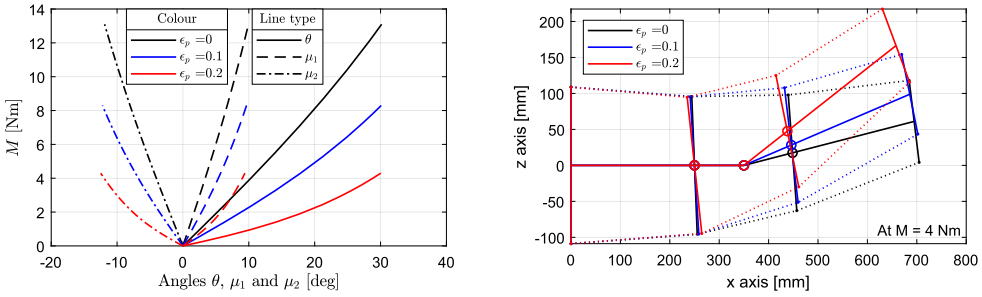

(a) Equilibrium plot (b) Deformed shape

Fig. 9. Variation of folding stiffness and the deformed shape with the change in the applied pre-strain for a 50-degree flare angle. (For interpretation of the colours in the figure(s), the reader is referred to the web version of this article.)

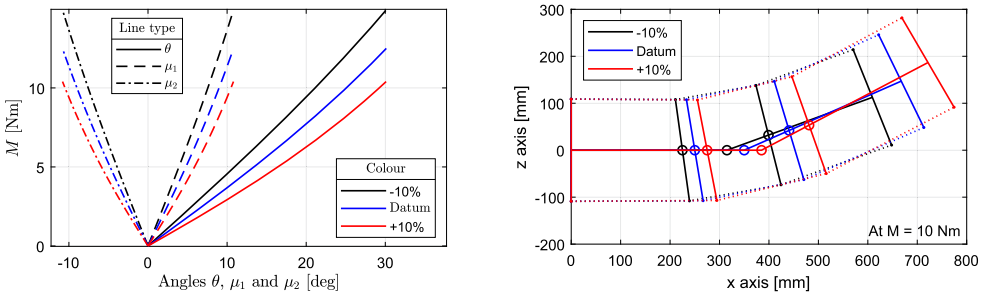

(a) Equilibrium plot (b) Deformed shape

Fig. 10. Variation of folding the stiffness and the deformed shape with the change in the length of spanwise beams. (For interpretation of the colours in the figure(s), the reader is referred to the web version of this article.)

This means that an increasing incremental gain in the applied moment is required for every unit increase in the folding angle. It is suspected that this may be a result of the pre-strain on the skin. In the unloaded configuration, both the upper and lower skin has the same amount of tension due to the applied pre-strain. While the tension on the upper skin favours an increase in the folding angle, the tension on the lower skin equally resists it. However, as the folding angle increases under external loading, the tension on the upper skin decreases while the tension on the lower skin increases. Consequently, for every unit increase in the folding angle, it results in an increasing incremental gain in resistance against further folding. This is seen in Fig. 8a as stiffening of the fairing with increasing folding angles.

5.3. Pre-strain

The effect of pre-strain on the stiffness and the deformed shape of the fairing is studied further for the 50-degree flare angle configuration in Fig. 9. Note that the constraint on the skin of being in tension was relaxed for this study. Hence, for low values of applied pre-tension and at large folding angles, the top skin can experience compressive strains. Fig. 9a shows that high pre-tension results in a softer stiffness for both folding and rib rotation. This indicates that the high out-of-plane stiffness of the skin due to pre-tension could be achieved together with the improved load alleviation characteristics of the wingtip due to reduced folding stiffness.

The decrease in folding stiffness with increasing pre-strain could be explained by the following approximate expression – which indicates that for a positive folding angle, the tension on the bottom skin opposes further folding (i.e., increase the torque) while the tension on the top skin favours it.

$$M \propto u_b\, d_b - u_t\, d_t \tag{10}$$

The term d_t and d_b are the distance from the hinge to the top and bottom skin. Note from Equation (6) that the displacement term has a component due to folding deformation and applied pre-strain. Hence, the expression could be re-arranged to the form

$$M \propto \left(u_{d_b}\, d_b - u_{d_t}\, d_t\right) - u_p\left(d_t - d_b\right) \tag{11}$$

where u_d is the displacement due to folding and u_p is the displacement due to pre-strain. The positive stiffness in the case with zero pre-strain indicates that the first term of the expression is positive. The deformed shape in Fig. 9b shows that $d_t > d_b$ for positive folding angles. Hence, any increase in pre-strain will reduce the folding stiffness of the system.

The 9a also shows that lower values of pre-tension result in a more linear stiffness in both folding and rib rotation. In contrast, cases with high pre-tension are shown to have increasing gradients at higher angles. This indicates the stiffening of the slice as the folding angle increase. This behaviour is seen for both the folding stiffness and the rib rotation stiffness. The deformed shape of the fairing with different pre-strain and the same applied moment is shown in Fig. 9b.

5.4. Beam length

The effect of changing the length of the spanwise beams on the folding response of the fairing was also analysed. Fig. 10a shows the softening of the fairing as the length of the spanwise sections increase. This is a result of inverse proportionality between the stiffness of the skin and its length, as expressed in Equation (2). Similarly, it also shows the softening of the rib rotational stiffness as the length of the beams is increased. The deformed shape of the fairing with different lengths of the spanwise beams are shown in Fig. 10b. It shows that a longer fairing results in a greater change in the distance from the folding hinge to the upper and the lower skin. The intersection of the folding hinge with the lower skin is determined by the folding angles θ, μ_1 and μ_2; and the ratio of the length of beams and the height of the ribs in the central rib-bay (i.e. l_{ai}/l_{ri} for $i \in [2, 3]$). If the length of the beams is longer than the height of the ribs in this region, the folding hinge will

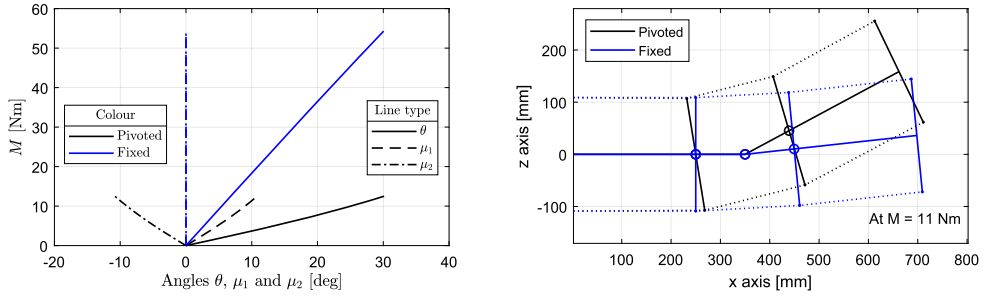

(a) Equilibrium plot (b) Deformed shape

Fig. 11. Variation of folding the stiffness and the deformed shape for fixed and pivoted rib configuration. (For interpretation of the colours in the figure(s), the reader is referred to the web version of this article.)

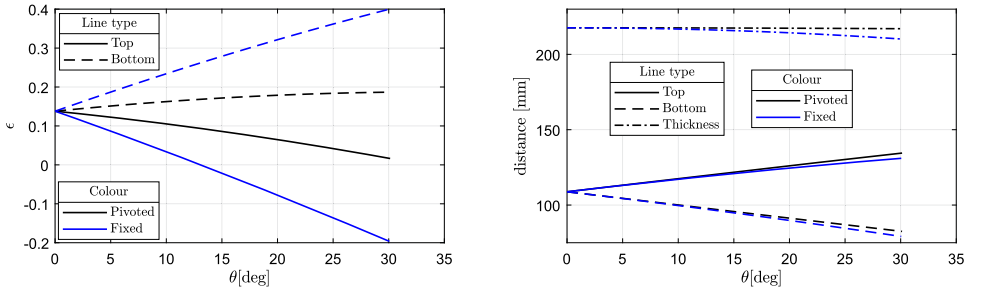

(a) Strain on the skin of mid-bay (b) Distance between hinge and skin, and the thickness of the section across the hinge

Fig. 12. Variation of the skin strain in mid-bay, the distance between the skin and the folding hinge, and section thickness across the hinge for fixed and pivoted rib configuration. (For interpretation of the colours in the figure(s), the reader is referred to the web version of this article.)

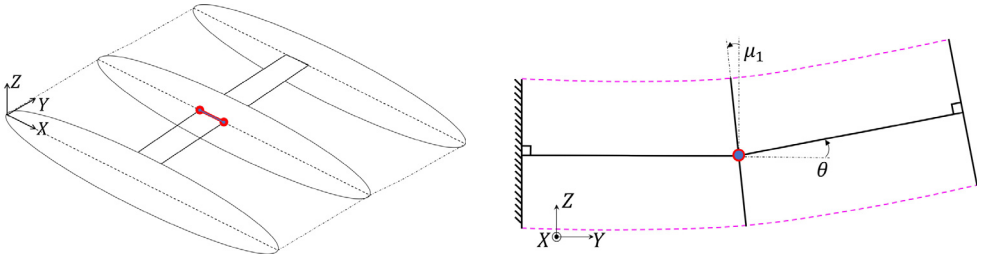

(a) Isometric view of the joint (b) Rear view (YZ-plane) of the joint

Fig. 13. An alternative configuration of the pivoting-rib based fairing concept. (a) shows the inboard rib that is joined to the outboard rib via a hinged joint (referred to as the folding hinge). The hinge of the central pivoting-rib is co-located and aligned with the folding hinge. (b) shows the rear view of the joint at a folding angle of θ and rotation angle of the rib μ_1.

intersect with the lower skin at higher folding angles. Hence, it is desirable to keep the length of the beams less than the height of the ribs in the central rib-bay (i.e. l_{ai}/l_{ri} for $i \in [2, 3] < 1$).

5.5. Comparison of fixed and pivoted rib configuration

Finally, a comparison study was made between the fixed and pivoted rib configurations. Fig. 11a shows that the fixed rib configuration is significantly stiffer in folding than the pivoted rib configuration. This is due to the absence of rotational degree of freedom of the ribs which results in a shorter length of the skin being engaged in the deformation – in this case, only the skin in the central rib-bay. In contrast, in the pivoted rib configuration the skins of the adjacent rib-bays are also involved in the deformation via the rotation of the ribs. The deformed shape of the slice in both fixed and pivoted rib configurations under the same loading is shown in Fig. 11b.

In addition to the reduced folding stiffness, the pivoted rib configuration also reduces the strain on the skin. Fig. 12a shows the variation of the strain in the skin of the mid rib-bay for both configurations. The increase in strain in the bottom skin and the decrease in strain in the top skin are both significantly higher for the fixed rib configuration. Consequently, the fixed rib configuration shows an earlier onset of compressive strain on the top skin, which is undesirable as it would be prone to wrinkling. Moreover, the change in the shortest distance between the skin and the folding hinge is shown in Fig. 12b. It shows a slower reduction in the distance between the bottom skin and the folding hinge for the pivoted rib configuration. Additionally, it also shows that the thickness of the section across the hinge is better retained by the pivoted rib configuration. However, it must be noted that the model used here does not account for bending deformation of the skin – hence, the model is limited in terms of the conclusions that could be derived from it. Nonetheless, the difference between the configurations is not significant in this case, though it shows an advantageous behaviour for the pivoted rib configuration over the fixed rib configuration.

5.6. Further improvements

The contact between the folding hinge and the lower skin could be avoided by using a different configuration of the pivoting-rib fairing concept where a pivoting central rib is co-located with the folding hinge. Fig. 13a shows the isometric view of the fairing with

the co-located folding hinge and the rotating central rib. Fig. 13b shows the rotation angle of the rib μ_1 which is free to rotate independent of the folding angle θ. The interaction of the rotation angle of the rib μ_1 and the folding angle θ is only through the reaction forces on the skin. The central rib maintains the distance of the rib height between the hinges and the skin, thereby, avoiding contact at all feasible folding angles. This enforcement of a constant distance between the hinge and the skin, however, could introduce localised out-of-plane deformation of the skin in both the rib-bays adjacent to the central rib. This could take the form of wrinkling on the skin at high folding angles. Future work on this concept would explore this behaviour and possible remedies to counter it through the design of skin architectures. These could take the form of spatially varying stiffness on the skin, particularly through the use of sandwich panels with cellular cores.

6. Conclusions

This paper demonstrates the working mechanics of a novel morphing fairing based on a pivoting-rib architecture and compliant skin. The fairing presented is a secondary morphing device that is aimed at minimising the coupling between the folding stiffness of the fairing and the out-of-plane stiffness of the skin. It provides a mechanism for re-distributing the localised skin deformation incurred during the folding of the joint over a greater length of the skin. This minimises the maximum skin strain for a given folding angle, thereby, improving the viability of the skin structure. The preliminary analysis of a simplified representative geometry presented in this paper provided a qualitative understanding of the deformation mechanics. It showed that the in-plane stiffness of the skin increases the folding stiffness of the fairing, while the pre-strain on the skin decreases the folding stiffness. It also showed the nonlinearity in the stiffness introduced by both the asymmetry in the geometry and the pre-strain on the skin. Moreover, it showed a decrease in the folding stiffness as a result of increasing the deformable length of the skin. The results demonstrate the benefit of the pivoting-rib fairing concept in minimising the strain on the skin while achieving a large range of deformation. Thus, this work shows the promise of the pivoting-rib concept for compliance-based morphing devices on folding joints. Future work on the concept should consider the 3-dimensional effects of the fairing through a finite element based model, including a study of the effect of various design parameters on the folding stiffness. Additionally, further studies would need to be carried out on the design of skin panels and its fatigue life; and the effects of aerodynamic loading on the skin deformation and the overall deformation of the joint.

Declaration of competing interest

The authors declare that they have no known competing financial interests or personal relationships that could have appeared to influence the work reported in this paper.

Data availability

No data was used for the research described in the article.

Acknowledgements

The authors acknowledge the following financial support for the research, authorship, and/or publication of this article. N.M. Mahid was supported by the Commonwealth Scholarship Commission (Reference Number MVCS-2016-350) in form of an undergraduate scholarship and EPSRC Centre for Doctoral Training in Composites Science, Engineering and Manufacturing (Grant Number EP/S021728/1) in form of the funding for his doctoral studies. B.K.S. Woods acknowledges the support of the Engineering and Physical Sciences Research Council (EPSRC) as part of the Early Career Fellowship, AdAPTS: Adaptive Aerostructures for Power and Transportation Sustainability (Grant Number EP/T008083/1).

References

[1] S. Barbarino, O. Bilgen, R.M. Ajaj, M.I. Friswell, D.J. Inman, A review of morphing aircraft, J. Intell. Mater. Syst. Struct. 22 (9) (2011) 823–877, https://doi.org/10.1177/1045389x11414084.
[2] J.J. Joo, B. Sanders, T. Johnson, M.I. Frecker, Optimal actuator location within a morphing wing scissor mechanism configuration, in: SPIE, 2006.
[3] T. Ivanco, R. Scott, M. Love, S. Zink, T. Weisshaar, Validation of the Lockheed Martin morphing concept with wind tunnel testing, in: American Institute of Aeronautics and Astronautics, 2007.
[4] R.M. Ajaj, M.S. Parancheerivilakkathil, M. Amoozgar, M.I. Friswell, W.J. Cantwell, Recent developments in the aeroelasticity of morphing aircraft, Prog. Aerosp. Sci. 120 (2021) 100682, https://doi.org/10.1016/j.paerosci.2020.100682.
[5] V.H. Siddaramaiah, D.E. Calderon, J.E. Cooper, T. Wilson, Preliminary studies in the use of folding wing-tips for loads alleviation, in: Royal Aeronautical Society Applied Aerodynamics Conference, Bristol, UK, 2014.
[6] A. Castrichini, Parametric Assessment of a Folding Wing-Tip Device for Aircraft Loads Alleviation, Phd thesis, University of Bristol, 2017, https://bris.on.worldcat.org/oclc/1052838653.
[7] A. Castrichini, V.H. Siddaramaiah, D.E. Calderon, J.E. Cooper, T. Wilson, Y. Lemmens, Preliminary investigation of use of flexible folding wing tips for static and dynamic load alleviation, Aeronaut. J. 121 (1235) (2016) 73–94, https://doi.org/10.1017/aer.2016.108.
[8] R.C.M. Cheung, D. Rezgui, J.E. Cooper, T. Wilson, Testing of a hinged wingtip device for gust loads alleviation, J. Aircr. 55 (5) (2018) 2050–2067, https://doi.org/10.2514/1.c034811.
[9] B.K.S. Woods, L. Parsons, A.B. Coles, J.H.S. Fincham, M.I. Friswell, Morphing elastically lofted transition for active camber control surfaces, Aerosp. Sci. Technol. 55 (2016) 439–448, https://doi.org/10.1016/j.ast.2016.06.017.
[10] J.E. Cooper, I. Chekkal, R.C.M. Cheung, C. Wales, N.J. Allen, S. Lawson, A.J. Peace, R. Cook, P. Standen, S.D. Hancock, G.M. Carossa, Design of a morphing wingtip, J. Aircr. 52 (5) (2015) 1394–1403, https://doi.org/10.2514/1.c032861.
[11] C. Thill, J. Etches, I. Bond, K. Potter, P. Weaver, Morphing skins, Aeronaut. J. 112 (1129) (2008) 117–139, https://doi.org/10.1017/s0001924000002062.
[12] C.S. Kothera, B.K. Woods, N.M. Wereley, P.C. Chen, E.A. Bubert, Cellular support structures used for controlled actuation of fluid contact surfaces, U.S. Patent No. 7,931,240, Apr. 26, 2011.
[13] R.D. Vocke, C.S. Kothera, B.K. Woods, N.M. Wereley, Development and testing of a span-extending morphing wing, J. Intell. Mater. Syst. Struct. 22 (9) (2011) 879–890, https://doi.org/10.1177/1045389x11411121.
[14] T. Yokozeki, S.-i. Takeda, T. Ogasawara, T. Ishikawa, Mechanical properties of corrugated composites for candidate materials of flexible wing structures, Composites, Part A, Appl. Sci. Manuf. 37 (10) (2006) 1578–1586, https://doi.org/10.1016/j.compositesa.2005.10.015.
[15] Y. Shan, C. Bakis, Flexible matrix composite actuators, in: 20th Technical Conference of the American Society for Composites, 2005, pp. 1712–1731, Conference date: 07-09-2005 through 09-09-2005.
[16] B.K.S. Woods, M.I. Friswell, Preliminary investigation of a fishbone active camber concept, in: Volume 2: Mechanics and Behavior of Active Materials; Integrated System Design and Implementation; Bio-Inspired Materials and Systems; Energy Harvesting, American Society of Mechanical Engineers, 2012.
[17] M. Powell, A Fortran subroutine for solving systems of nonlinear algebraic equations, techreport AERE-R-5947, Atomic Energy Research Establishment, Harwell, England (United Kingdom), Nov. 1968, https://www.osti.gov/biblio/4772677.
[18] International Civil Aviation Organization, Annex 14 – Aerodromes – Volume I – aerodromes design and operations, https://store.icao.int/en/annex-14-aerodromes, Jul. 2004.
[19] Federal Aviation Administration, FAA Advisory Circular 18150/5300-13B – airport design, https://www.faa.gov/airports/resources/advisory_circulars/index.cfm/go/document.current/documentnumber/150_5300-13, Mar. 2022.